J. Ocean Univ. China (Oceanic and Coastal Sea Research)
DOI 10.1007/s11802-017-3153-7
ISSN 1672-5182, 2017 16 (2): 184-190
http://www.ouc.edu.cn/xbywb/
E-mail:xbywb@ouc.edu.cn

Observation of Near-Inertial Internal Waves on the Continental Slope in the Northwestern South China Sea

ZHENG Jie, TIAN Jiwei, and LIANG Hui*

Physical Oceanography Laboratory, *Ocean University of China*, *Qingdao* 266100, *P. R. China*

(Received March 14, 2016; revised May 18, 2016; accepted November 10, 2016)

Abstract Based on nearly 3 months of moored acoustic Doppler current profiler records on the continental slope in the northwestern South China Sea (SCS) in 2006, this study examines temporal and vertical characteristics of near-inertial internal waves (NIW). Rotary frequency spectrum indicates that motions in the near-inertial frequency are strongly polarized, with clockwise (CW) energy exceeding counterclockwise (CCW) by about a factor of 10. Wavelet analysis exhibits an energy peak exceeding the 95% confidence level at the frequency of local inertial during the passage of typhoon Xangsane (24 September to 4 October). This elevated near-inertial kinetic energy (NIKE) event possesses about a 4 days delay correlation with the time integral of energy flux induced by typhoon, indicating an energy source of wind. Further analysis shows that the upward phase velocity of this event is $3.8\,\mathrm{m\,h^{-1}}$ approximately, corresponding to a vertical wavelength of about 125 m if not taking the redshift of local inertial frequency into account. Rotary vertical wavenumber spectrum exhibits the dominance of clockwise-with-depth energy, indicating downward energy propagation and implying a surface energy source. Dynamical modes suggest that mode 1 plays a dominant role at the growth stage of NIW, whereas major contribution is from higher modes during the penetration of NIKE into the ocean interior.

Key words South China Sea; near-inertial internal waves; mooring

1 Introduction

Internal waves are a ubiquitous and significant phenomenon in the ocean. These waves with frequency near f are commonly referred to as near-inertial internal waves (NIW). Wind-forced, downward-propagating NIW are thought to be important to ocean turbulence and mixing because the near-inertial peak contains a substantial portion of the total kinetic energy in the internal waveband and is believed to dominate the vertical shear (Alford and Gregg, 2001). Hence, a better understanding of the sources and subsequent propagation of NIW seems warranted for parameterizing their effects in large-scale models.

Generally, observations and model experiments both indicated that the predominant generation mechanism of NIW is wind forcing (D'Asaro, 1985) by imparting momentum to the surface mixed layer (ML). The observed amplitude of NIW current in the ML was up to $1.5\,\mathrm{m\,s^{-1}}$ under Hurricane Frances (2004) in the Atlantic Ocean (Sanford *et al.*, 2011). An even stronger current response ($>2\,\mathrm{m\,s^{-1}}$) was reported by Teague *et al.* (2007) in the shelf and slope region of the Gulf of Mexico when Hurricane Ivan (2004) passed directly over the mooring array. Case studies of typhoon-induced near-inertial motions in the northwestern South China Sea (SCS) suggested that the amplitude of NIW current was about $0.4\,\mathrm{m\,s^{-1}}$ and the upward phase velocity was estimated to be $5.6\,\mathrm{m\,h^{-1}}$ (Chen *et al.*, 2013), larger than the result of $1.8\,\mathrm{m\,h^{-1}}$ estimated by Sun *et al.* (2011) in the northern SCS. Based on velocity and temperature profiles acquired in the western Gulf of Mexico, Shay *et al.* (1998) suggested that a summation of the first four baroclinic modes could describe up to 77% of near-inertial kinetic energy (NIKE) during the first 1.75 inertial periods, whereas the variance explained by this modal summation decreased to a minimum of 36% after 2.9 inertial periods.

The SCS is the largest marginal sea in the southeastern Asian waters. Due to the special geographic location and complex topography, many scales of motion are active in the SCS, including large-scale circulation (Su, 2004), mesoscale eddies (Zhang *et al.*, 2013), and particularly the strong internal tides (Xu *et al.*, 2013) and near-inertial oscillations (Guan *et al.*, 2014). The present study aims at a systematic investigation of NIW on the continental slope in the northwestern SCS.

The paper is organized as follows. Section 2 describes data and methods used in this study. Section 3 outlines the temporal variability and vertical distribution of NIKE. Section 4 pays special attention to the exceptionally high NIKE in late September and early October induced by a typhoon event. Finally, summary and discussion are given in Section 5.

* Corresponding author. Tel: 0086-532-66782367
E-mail: lhzy.1987@163.com

2 Data and Methods

2.1 Moored Data

The mooring was deployed at 19°59′N, 115°30′E in the northwestern SCS (see the red pentagram in Fig.1) from 17 August 2006 to 11 November 2006. Water depth at this station was 1319 m. The mooring was equipped with upward-looking and downward-looking 75 kHz acoustic Doppler current profilers (ADCPs) at 640 m depth to measure the velocity from 46 to 1231 m. Each instrument sampled in 10 m bins and formed ensembles every 20 min, which were enough to record sufficient information on NIW. Given that the real-time pressure information of the instruments was recorded by the two ADCPs, all the velocity data were first linearly interpolated onto uniform levels at 5 m intervals.

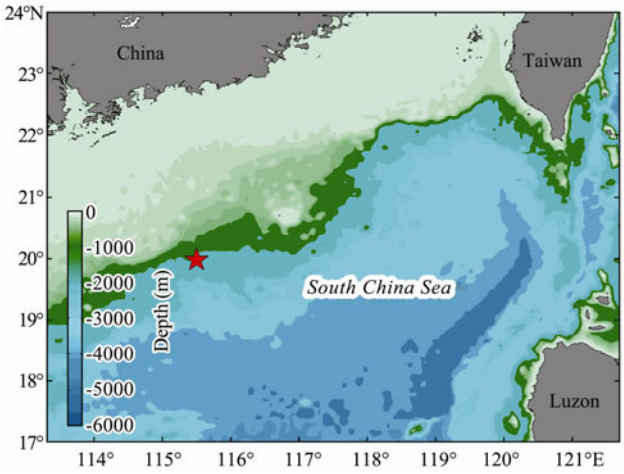

Fig.1 Map of northern South China Sea with bathymetry contours. The red pentagram indicates the location of the mooring.

The upper 0.3% and lower 8.4% of the profiling range of the ADCPs were discarded because of contamination by the boundary reflection of the sidelobe transmission, *i.e.*, velocity records used in this study were covering water column from 50 to 1130 m. Baroclinic current was obtained after subtracting depth-averaged flow, which was regarded as barotropic current approximately.

2.2 WKB Scaling

Internal waves adjust their wavenumber and amplitude as they undergo refraction in depth-varying stratification. To minimize these effects, it is necessary to apply Wentzel-Kramers-Brillouin (WKB) scaling following Leaman and Sanford (1975). Thus, we multiply baroclinic current profiles by a factor of $[N(z)/\bar{N}]^{-1/2}$, where climatological buoyancy frequency N is derived from the World Ocean Atlas 2013 (WOA13) monthly temperature and salinity data (0.25° resolution) at the mooring location. The depth-mean stratification $\bar{N}$, averaged between 0 and 1315 m, are 7×10^{-3}, 7×10^{-3}, 6.8×10^{-3}, and 6.5×10^{-3} rad s^{-1} in August, September, October, and November, respectively.

To account for wavenumber changes, WKB-stretched depth (Fig.5a) is computed as

$$\tilde{z}(z,t)=\int_0^z \frac{N(z)}{\bar{N}}\mathrm{d}z\,. \tag{1}$$

It is important to clarify that the depth-time maps are plotted versus unstretched depth, but quantitative calculation such as the rotary vertical wavenumber spectrum is computed in stretched coordinates.

2.3 Slab Model

The slab model has been widely used and validated for producing realistic simulation of the near-inertial current response to impulsive wind events (Pollard, 1980; Alford, 2001). We examine the ML flux by running the Pollard and Millard (1970) slab model forced with European Center for Medium-Range Weather Forecasts (ECMWF) wind (0.125° resolution, 6-hourly output) at the location and period of the mooring (Fig.3a). The work done by the wind on ML motions can most directly be computed as the dot product of the wind stress and ML current,

$$\Pi=\vec{\tau}\cdot\vec{u}\,. \tag{2}$$

Equations for eastward and northward components of ML current are as follows:

$$\begin{cases}\dfrac{\partial u}{\partial t}-fv=\dfrac{\tau_x}{\rho_0 H}-ru\\[2ex] \dfrac{\partial v}{\partial t}+fu=\dfrac{\tau_y}{\rho_0 H}-rv\end{cases}, \tag{3}$$

where f is the local inertial frequency, τ_x and τ_y are the wind stress components, ρ_0=1024 kg m^{-3} is the reference density of seawater, H is the ML depth, and r=0.15f (Alford, 2001) is an empirical damping coefficient parameterizing the decay of ML near-inertial current. In the present study, potential density is derived from WOA13 monthly temperature and salinity data as well. H is then calculated following the usual convention, which define H as the first depth where the measured potential density exceeding the surface value by 0.125 kg m^{-3}.

Based on the 10 m height wind velocity vector $\vec{u}_{10}$ from ECMWF, the wind stress field $\vec{\tau}$ is computed *via* Eq. (4):

$$\vec{\tau}=\rho_a C_D U_{10}\vec{u}_{10}\,, \tag{4}$$

where ρ_a=1.3 kg m^{-3} is the air density. The drag coefficient C_D adopts the formula proposed by Oey *et al.* (2006) defined as

$$C_D\times1000=\begin{cases}1.2, U_{10}\le11\ \mathrm{m\ s^{-1}}\\ 0.49+0.065U_{10}, 11<U_{10}\le19\ \mathrm{m\ s^{-1}}\\ 1.364+0.0234U_{10}-0.00023158, 19<U_{10}\le100\ \mathrm{m\ s^{-1}}\end{cases}, \tag{5}$$

which fits the Large and Pond (1981) formula at low wind speed and the Powell *et al.* (2003) formula at high wind

speed.

3 Characteristics of NIKE

3.1 Rotary Frequency Spectrum

Rotary spectrum analysis is a proven method for interpretation of geophysical flows exhibiting inherent rotational characteristics (Gonella, 1972). Negative and positive frequencies in rotary frequency spectrum are corresponding to clockwise (CW) and counterclockwise (CCW) motions, respectively. It is possible to readily distinguish between CW and CCW effects since the spectrum is asymmetric about zero frequency. We therefore exhibit the rotary frequency spectrum in Fig.2. To facilitate comparison, the horizontal axis is unified into absolute values of frequencies.

Rotary frequency spectrum of the depth-averaged WKB-scaled baroclinic velocity is given in Fig.2a. It is obvious that significant peaks in the spectrum occur at near-inertial (−0.68 cpd), diurnal (±0.96 cpd) and semidiurnal (±1.97 cpd) frequencies, showing similar polarization with CW energy more than 10 times greater than CCW, which means the horizontal current vectors in the internal waveband mainly rotate CW. As a result, we show the CW component of the rotary frequency spectrum of WKB-scaled baroclinic velocity at each depth in Fig.2b. After WKB scaling, CW motions in near-inertial frequency are evident in full depth and even stronger than those in semidiurnal tidal frequency in upper 400 m water column.

NIW are isolated by applying a fourth-order Butterworth filter to the baroclinic current. Upper and lower limits are {0.85, 1.15}f (Fig.2a, blue shading), similar to Xie *et al.* (2011) and Chen *et al.* (2013).

3.2 Wind Work and Kinetic Energy

Following bandpassing, NIKE (Fig.3c) is computed straightforward *via* Eq. (6):

$$NIKE = \frac{1}{2}\rho_0 (u_f^2 + v_f^2), \tag{6}$$

where u_f and v_f are the filtered eastward and northward components of NIW current. To evaluate its life, the depth-averaged NIKE is further low-pass filtered with local inertial period (about 35 h) and is overplotted in Fig.3c (magenta curve). The scale is placed at the right axis.

Accompanied with the intermittent input of energy from the wind in Fig.3b, pronounced near-inertial signals are also intermittent. Increases in NIKE generally follow strong forcing events, as expected, but correspondence is not perfect between forcing amplitude and the response. For example, the maximum NIKE in late September and early October increase sharply just after typhoon Xangsane. However, a similar increase in 18 August occurs in a time of more moderate forcing. The variability likely arises from differences in the lateral structure of the storms and mesoscale currents during the various events, which are of course not resolved by our single mooring.

Further, it is notable that the cumulative energy induced by wind and the transient energy appearing at the near-inertial frequency are strongly correlated in time during the passage of typhoon Xangsane (24 September to 4 October). Under the continuous influence of this wind event, NIW originate in 28 September, and then peak rapidly in 3 October with significant enhancement by a factor of 2–3. Thereafter, NIKE damps quickly and almost disappears in 8 October. Lag correlation analysis

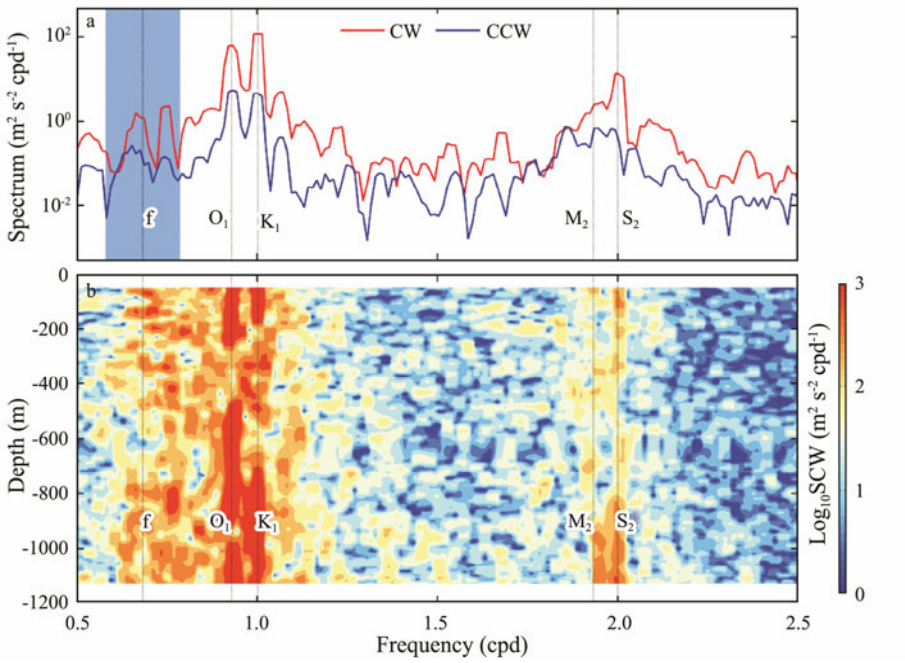

Fig.2 (a) Rotary frequency spectrum of the depth-averaged WKB-scaled baroclinic velocity showing the CW (red line) and CCW (blue line) components. The near-inertial band of {0.85, 1.15}f is shaded in blue. (b) Rotary frequency spectrum of WKB-scaled baroclinic velocity *vs.* depth, zoomed in the CW internal waveband. Frequencies of f, O_1, K_1, M_2 and S_2 are indicated as thin vertical lines.

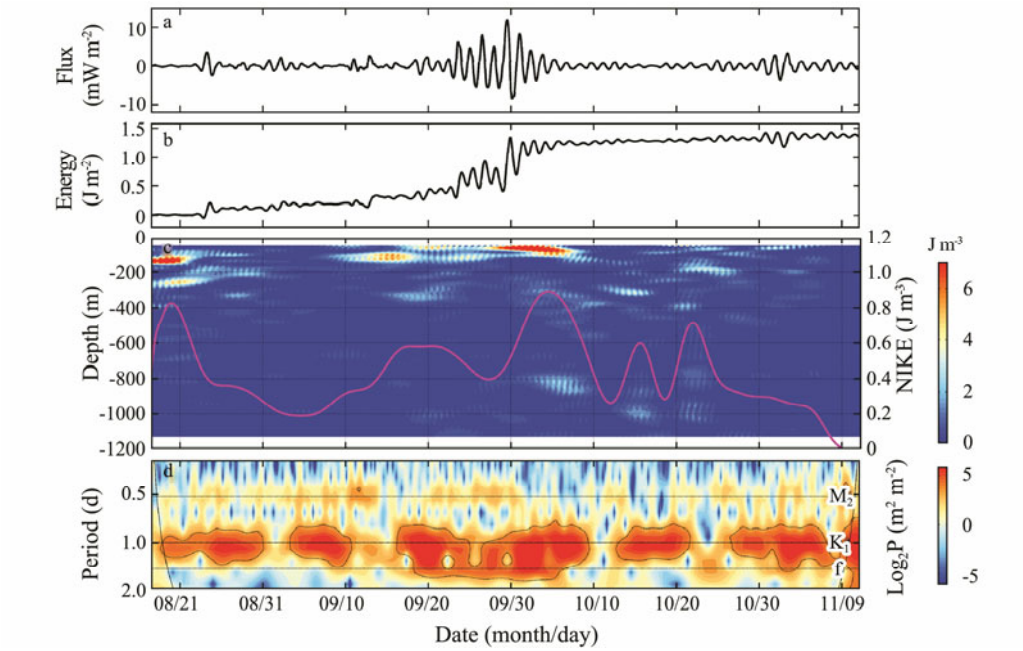

Fig.3 (a) Wind-induced energy flux to NIW in the surface ML. (b) The time integral of the wind-induced energy flux. (c) Temporal variability and vertical distribution of NIKE at the mooring site. The magenta curve represents low-frequency component of the depth-averaged NIKE obtained by low-pass filter with local inertial period. (d) Wavelet power spectra (color contours) of northward component of baroclinic current for mooring at 65 m depth. Black curve represents 95% confidence level. Thin horizontal lines indicate the *f*, K_1 and M_2 frequencies.

between the wind-induced energy flux and the depth-averaged NIW current (not shown) further demonstrates that NIW exhibit about a 4 days delay correlation with wind work, which implies the maximum NIKE event is mainly induced by wind forcing.

In order to obtain a complete timescale representation of localized and transient phenomena occurring at different time-scales, we analyzed the wavelet spectrum following Torrence and Compo (1998) using the northward component of baroclinic current at the depth of 65 m (Fig.3d). It is striking that energy at near-inertial frequency becomes more energetic and a strong energy peak exceeding the 95% confidence level at the frequency of *f* appears during the passage of typhoon Xangsane. Therefore, we will pay special attention to this exceptionally high NIKE in the next Section.

4 The Maximum NIKE Event

4.1 Phase Velocity and Vertical Wavelength

The maximum NIKE during the study period is observed in late September and early October, induced by Typhoon Xangsane. Figs.4a and 4b show the time series of NIW current profiles from 25 September to 10 October. The magnitude of the oscillation is about 15 cm s^{-1} for both eastward and northward current components. Based on the slope of the NIW current profiles, the phase velocity is estimated to be 3.8 m h^{-1} approximately. With the period of 33 h estimated from the adjacent positive (or negative) phase, the vertical wavelength is about 125 m. Actually, we underestimate the vertical wavelength because the warm mesoscale eddy at this period leads redshift to the local inertial frequency. Another interesting phenomenon is the NIW current has an upward propagating phase, indicating the vertical component of group velocity is downgoing, *i.e.*, NIKE propagates downward into the thermocline.

A set of discrete downward and rightward swaths (Fig.4c) also illustrate substantial energy penetrating deep in the record. The influence of NIW reaches the depth of 80 m in 1 October, and then extends to 90 m depth in 3 October with the vertical group velocity of about 5 m d^{-1}. Thereafter, vertical component of the group velocity has a slight increase according to the slope of the NIKE pattern. However, NIW only affect water column up to 120 m eventually due to the decay of NIKE.

4.2 Rotary Vertical Wavenumber Spectrum

Eastward and northward components of WKB-scaled NIW current profile at 0 o'clock of 3 October are presented in Fig.5b. After WKB scaling, velocity amplitudes in thermocline shrink to less than 8 cm s^{-1}, close to that in deep water (*e.g.*, eastward component at 800 m depth). Rotary vertical wavenumber spectrum of this profile is examined next (Fig.5c). CW and CCW components are associated with downward and upward energy propagation, which are plotted separately with red and blue lines, respectively.

As shown in Fig.5c, with the increase of the vertical wavenumber, the spectral energy declines slowly for vertical scale larger than 100 m and drops sharply after that. Vertical scales on 1000 m are 10 and 3 times stronger than those on 100 m for CW and CCW components, which implies signals in NIW are most prominent for motions at larger scale. In addition, on vertical scale of 1000 m, the downward spectral energy is 9.3 times larger than the

upward, whereas the difference reduces to 3.4 times on the vertical scale of 100 m. This result signifies near-inertial motions are dominated by CW turning, denoting downward energy propagation and implying a surface energy source, which is consistent with the results of Figs.3c and 4a–c.

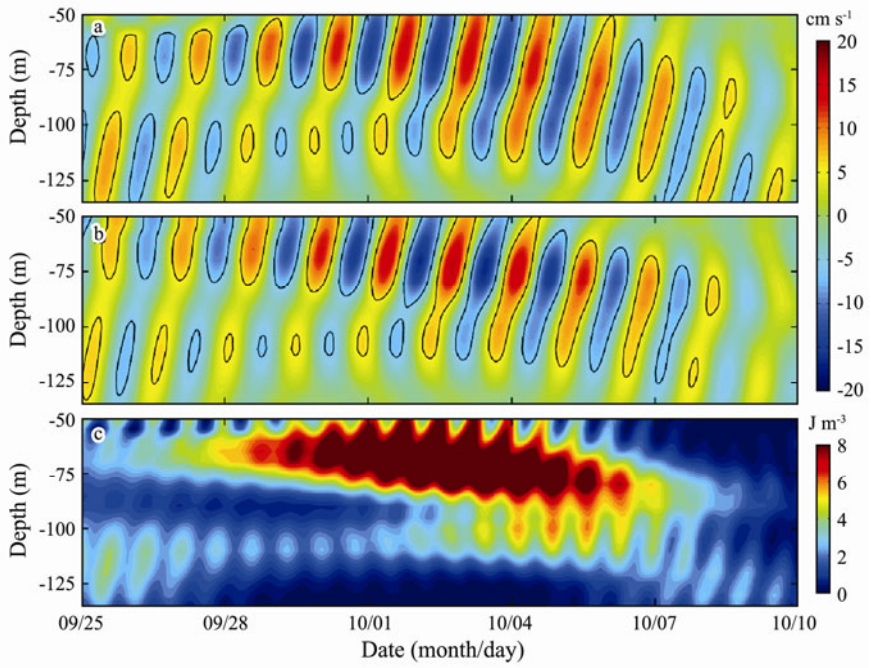

Fig.4 Time series of the (a) eastward and (b) northward components of the NIW current profiles from 25 September to 10 October. Black contours mark the velocity of ±6 cm s^{-1}. (c) Time evolution of NIKE during the same period.

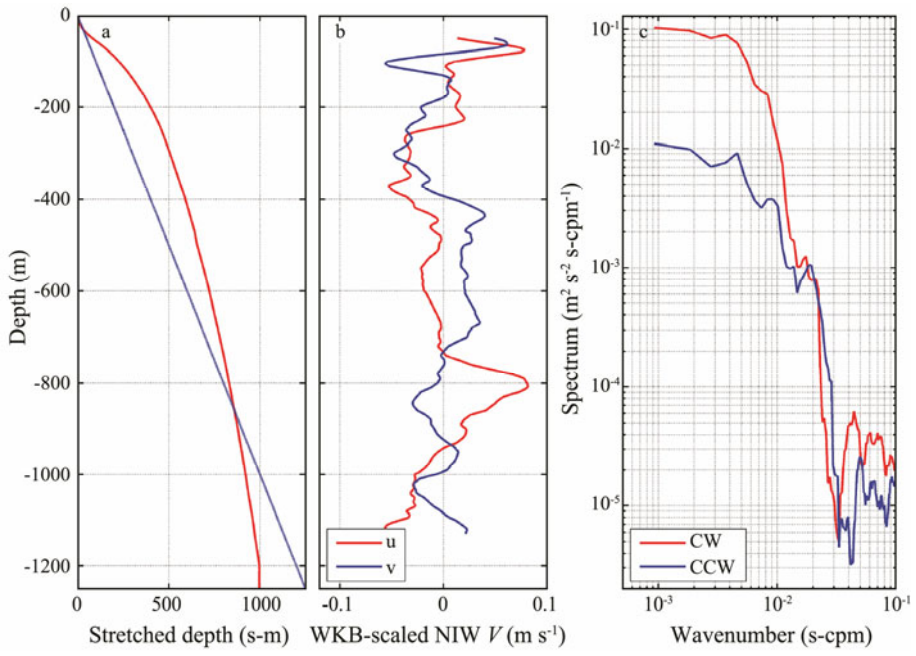

Fig.5 (a) WKB-stretched depth (red line). The dashed blue line shows the unstretched depth for reference. (b) Eastward (red line) and northward (blue line) components of WKB-scaled NIW current profile at 0 o'clock of 3 October. (c) Rotary vertical wavenumber spectrum of the profile showing the CW turning with depth component (red line) and the CCW component (blue line). Data have been WKB stretched and scaled.

4.3 Dynamical Modes

To understand the penetration of NIKE into the ocean interior, the eastward and northward components of NIW current are expanded in terms of the vertical normal modes (Gill, 1984):

$$\boldsymbol{u}_f(z,t) = \sum_{n=0}^{N} \boldsymbol{u}_n(t)\Phi_n(z)\,, \tag{7}$$

where $\Phi_n(z)$ are the eigenfunctions of the Sturm-Liouville problem (Flierl, 1978):

$$\frac{\mathrm{d}^2\Phi_n(z)}{\mathrm{d}z^2}+\frac{N^2(z)}{c_n^2}\Phi_n(z)=0\,. \tag{8}$$

Fig.6a shows the depth-averaged NIKE from 50 to 120 m for the first nine modes. It is notable that mode 1 plays a dominant role at the growth stage of the maximum NIKE event (28 September to 3 October as mentioned above). However, this stronger event is largely contributed by the higher vertical modes (mode 4, mode 6 and mode 8) during the period of decay (3 October to 8 October). We further exhibit the time-averaged NIKE profiles from 28 September to 8 October for mode 1, mode 2, mode 4, mode 6, and mode 8 in Fig.6b. The sum of these five modes reveals the general characteristics of NIKE shown in Fig.6c, with description of up to 78% at the depth of 50 m and less than 50% at about 80 m depth. In addition, it is obvious that the maximum NIKE in the deeper layer (*e.g.*, from 70 to 90 m) correlated with the decay period is mainly captured by mode 6 and mode 8, consistent with Fig.6a. This is mainly because the first mode usually propagates faster than the other higher modes due to its longer vertical wavelength. As a result, it quickly leaves the observation area whereas the rest higher modes stay at the location longer.

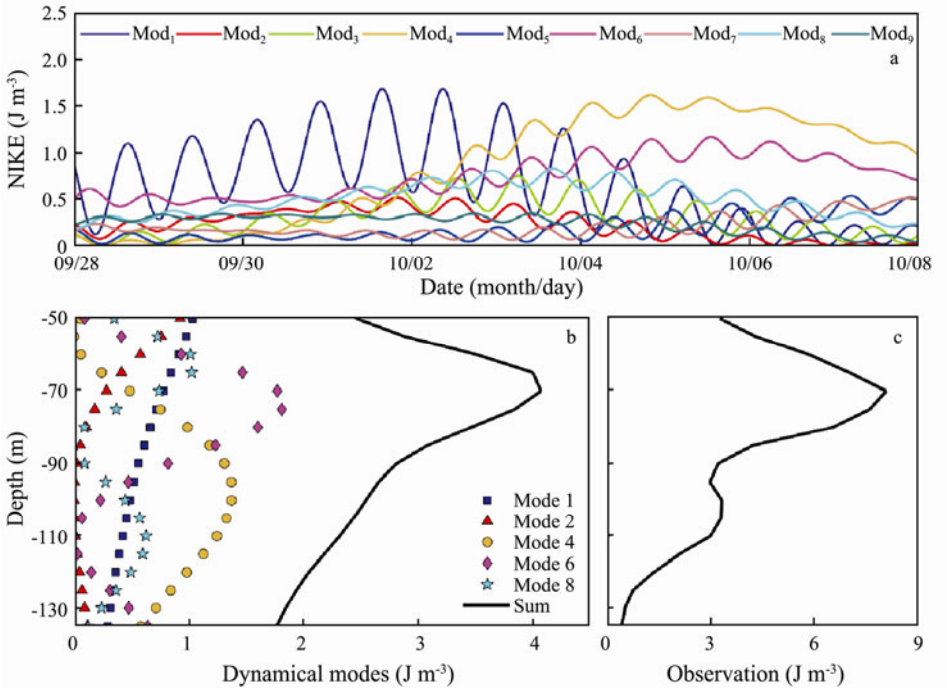

Fig.6 (a) The depth-averaged NIKE from 50 to 120 m for the first nine dynamical modes, distinguished with different colors. (b) The time-averaged NIKE from 28 September to 8 October for the baroclinic modes (n=1, 2, 4, 6, and 8) and the combination of these five modes (black line). (c) The time-averaged NIKE based on observation during the same period.

5 Summary and Discussion

Internal waves about the local near-inertial frequency are common in the global ocean and contribute greatly to oceanic mixing. Due to insufficient observation data, surveys of NIKE in the SCS have been limited. In this study, the temporal and vertical structures of NIW are investigated on the basis of nearly 3 months moored acoustic Doppler current profiler records on the continental slope in the northwestern SCS in 2006.

Rotary frequency spectrum illustrates significant peaks in the spectrum occurring at near-inertial frequencies, exhibiting polarization with CW energy more than 10 times greater than CCW. Wavelet analysis shows a strong energy peak exceeding the 95% confidence level at the frequency of local inertial during the passage of typhoon Xangsane. This elevated NIKE event possesses about a 4 days delay correlation with wind work done by typhoon, indicating an energy source of wind.

Further analysis demonstrates that the upward phase velocity and vertical wavelength of this event are approximately 3.8 m h^{-1} and 125 m, respectively. However, we underestimate the vertical wavelength because of the neglecting of the redshift of local inertial frequency. Rotary vertical wavenumber spectrum exhibits a dominance of clockwise-with-depth energy, indicating downward energy propagation and implying a surface energy source. Dynamical modes suggest that NIW are largely contributed by mode 1 originally, whereas higher modes turn to dominate NIKE as NIW propagate downward.

The SCS experiences frequent typhoon events, variable hydrographic structure and circulation because of the alternating monsoon winds. With different topography, oceanic stratification, background flow, and atmospheric forcing, NIW may have different characteristics. Therefore, to clarify the behavior and finally predict the occurrences of NIW in the SCS, further efforts including field

observations and numerical modeling are necessary.

Acknowledgements

This work is supported by the National Key Basic Research Program of China (Program 973) (Grant No. 2014 CB745003), the National Key Scientific Instrument and Equipment Development Project (Grant No. 2012YQ120 03909), the National High Technology Research and Development (863) Program of China (Grant Nos. 2013AA 09A502, 2013AA09A501), and the Global Change and Air-Sea Interaction Project (Grant No. GASI-03-01-01-03). Insightful comments from anonymous reviewers are very helpful in improving the work.

References

Alford, M. H., 2001. Internal swell generation: The spatial distribution of energy flux from the wind to mixed layer near-inertial motions. *Journal of Physical Oceanography*, **31** (8): 2359-2368.

Alford, M. H., and Gregg, M. C., 2001. Near-inertial mixing: Modulation of shear, strain and microstructure at low latitude. *Journal of Geophysical Research*, **106** (C8): 16947-16968.

Chen, G., Xue, H., Wang, D., and Xie, Q., 2013. Observed near-inertial kinetic energy in the northwestern South China Sea. *Journal of Geophysical Research: Oceans*, **118** (10): 4965-4977.

D'Asaro, E. A., 1985. The energy flux from the wind to near-inertial motions in the surface mixed layer. *Journal of Physical Oceanography*, **15** (8): 1043-1059.

Flierl, G. R., 1978. Models of vertical structure and the calibration of two-layer models. *Dynamics of Atmospheres and Oceans*, **2** (4): 341-381.

Gill, A. E., 1984. On the behavior of internal waves in the wakes of storms. *Journal of Physical Oceanography*, **14** (7): 1129-1151.

Gonella, J., 1972. A rotary-component method for analysing meteorological and oceanographic vector time series. *Deep Sea Research and Oceanographic Abstracts*, **19** (12): 833-846.

Guan, S., Zhao, W., Huthnance, J., Tian, J., and Wang, J., 2014. Observed upper ocean response to typhoon Megi (2010) in the Northern South China Sea. *Journal of Geophysical Research: Oceans*, **119** (5): 3134-3157.

Large, W. G., and Pond, S., 1981. Open ocean momentum flux measurements in moderate to strong winds. *Journal of Physical Oceanography*, **11** (3): 324-336.

Leaman, K. D., and Sanford, T. B., 1975. Vertical energy propagation of inertial waves: A vector spectral analysis of velocity profiles. *Journal of Geophysical Research*, **80** (15): 1975-1978.

Oey, L. Y., Ezer, T., Wang, D. P., Fan, S. J., and Yin, X. Q., 2006. Loop current warming by Hurricane Wilma. *Geophysical Research Letters*, **33** (8): 153-172.

Pollard, R. T., 1980. Properties of near-surface inertial oscillations. *Journal of Physical Oceanography*, **10** (3): 385-398.

Pollard, R. T., and Millard, R. C., 1970. Comparison between observed and simulated wind-generated inertial oscillations. *Deep Sea Research and Oceanographic Abstracts*, **17** (4): 813-821.

Powell, M. D., Vickery, P. J., and Reinhold, T. A., 2003. Reduced drag coefficient for high wind speeds in tropical cyclones. *Nature*, **422** (6929): 279-283.

Sanford, T. B., Price, J. F., and Girton, J. B., 2011. Upper-ocean response to Hurricane Frances (2004) observed by profiling EM-APEX floats. *Journal of Physical Oceanography*, **41** (6): 1041-1056.

Shay, L. K., Mariano, A. J., Jacob, S. D., and Ryan, E. H., 1998. Mean and near-inertial ocean current response to Hurricane Gilbert. *Journal of Physical Oceanography*, **28** (5): 858-889.

Su, J., 2004. Overview of the South China Sea circulation and its influence on the coastal physical oceanography outside the Pearl River Estuary. *Continental Shelf Research*, **24** (16): 1745-1760.

Sun, Z., Hu, J., Zheng, Q., and Li, C., 2011. Strong near-inertial oscillations in geostrophic shear in the northern South China Sea. *Journal of Oceanography*, **67** (4): 377-384.

Teague, W. J., Jarosz, E., Wang, D. W., and Mitchell, D. A., 2007. Observed oceanic response over the upper continental slope and outer shelf during Hurricane Ivan. *Journal of Physical Oceanography*, **37** (9): 2181-2206.

Torrence, C., and Compo, G. P., 1998. A practical guide to wavelet analysis. *Bulletin of the American Meteorological Society*, **79** (1): 61-78.

Xie, X. H., Shang, X. D., Haren, H. V., Chen, G. Y., and Zhang, Y. Z., 2011. Observations of parametric subharmonic instability-induced near-inertial waves equatorward of the critical diurnal latitude. *Geophysical Research Letters*, **38** (5): 132-140.

Xu, Z., Yin, B., Hou, Y., and Xu, Y., 2013. Variability of internal tides and near-inertial waves on the continental slope of the northwestern South China Sea. *Journal of Geophysical Research: Oceans*, **118** (1): 197-211.

Zhang, Z., Zhao, W., Tian, J., and Liang, X., 2013. A mesoscale eddy pair southwest of Taiwan and its influence on deep circulation. *Journal of Geophysical Research: Oceans*, **118** (12): 6479-6494.

(Edited by Xie Jun)